Wind–wave interaction over a sloped beach: Turbulence and wave breaking

By J. Wang, H. Hwang AND C. Gorlé

We present a numerical study of wind-driven surface waves propagating over a sloped beach and flat platform using the two-phase large-eddy simulation (LES) solver. Six cases are considered, spanning zero to strong (0–30 m/s) wind speeds and short/long waves, to examine how wave breaking, turbulence, and surface shear velocity develop across the slope and onshore platform. High-fidelity simulations capture wave shoaling and breaking on the beach, generating near-surface turbulence. We analyze wave height attenuation, breaking onset, and the resulting turbulent airflow. A signal processing pipeline [Butterworth filters, wavelet/ensemble empirical mode decomposition (EEMD) and fast Fourier transform (FFT)] is used to separate high-frequency turbulence from mean flow and to compute energy spectra and integral length scales. Results show that shorter waves break earlier on the slope, producing stronger near-surface turbulence, whereas longer waves penetrate further shoreward before breaking. Increased wind speeds tend to enhance turbulence and reduce wave height through more vigorous breaking. Mean wind profiles adjust onshore of the breaker zone, with reduced shear and elevated turbulent intensities. Spectral analysis reveals energy transfer toward high frequencies after breaking, and integral length scales decrease downwind. Finally, a correlation-based regression links wave and wind parameters to turbulence metrics, highlighting the dominant influence of wind speed and wave age. These findings elucidate the coupled air–sea flow structure over a beach, with implications for coastal wind–wave modeling.

1. Introduction

Wind–wave interaction is central to air–sea momentum transfer, turbulence generation and the evolution of the marine boundary layer. Classic linear theories by Miles (1957) and Phillips (1957) predicted the onset of wave growth by shear and turbulent pressure fluctuations, respectively, while Charnock (1955) established a simple relation between surface roughness and wind stress. The drag dependence on sea state and the multiscale coupling between waves and wind have since motivated numerous studies. Nonlinear models and boundary-layer analyses have highlighted the role of wave-coherent airflow and phase-locked pressure, leading to modifications of the mean profile and drag coefficient (Belcher & Hunt 1993; Sullivan *et al.* 2000; Hara & Belcher 2004; Sullivan & McWilliams 2010). Investigations of breaking waves have demonstrated that dissipative wave events inject significant turbulence into the water column and modulate the airside stress (Phillips 1985; Melville 1996; Banner & Peirson 2007; Thomson *et al.* 2016).

Recent measurements and large-eddy simulations (LESs) have refined our understanding of the turbulent marine boundary layer. Field campaigns and numerical studies reveal spectral energy transfer and eddy structures over nonbreaking and breaking waves (Romero *et al.* 2012; Hao & Shen 2019; Larsen *et al.* 2019; Deskos *et al.* 2021). Breaking enhances high-frequency energy and alters integral scales; the wave age and nondimensional fetch (wind–wave interaction distance) emerge as key parameters (Popinet 2009;

Buckley & Veron 2016). Laboratory and numerical experiments further show that shorter waves lead to earlier shoaling and stronger near-surface turbulence, whereas longer waves penetrate further before breaking (Banner & Peirson 2007; Larsen *et al.* 2019). LESs of wind over broadband spectra continue to provide insight into vertical and streamwise structure and momentum exchange (Veron 2015; Hao & Shen 2019). The present study extends these works to a sloping bathymetry, combining modern two-phase numerics with regression analysis. It builds upon numerical techniques for interface capturing and turbulence modeling (Hirt & Nichols 1981; Brackbill *et al.* 1992; Weller *et al.* 1998; Scardovelli & Zaleski 1999; Rusche 2002), providing a comprehensive data set for wind–wave coupling across scales.

2. Methods

2.1. *Governing equations*

We use an incompressible two-phase volume-of-fluid (VOF) solver in OpenFOAM. The governing equations are $\nabla\cdot\mathbf{u} = 0$ and a single-fluid momentum equation for the mixture velocity,

$$\rho(\alpha)\left(\frac{\partial \mathbf{u}}{\partial t} + \mathbf{u}\cdot\nabla\mathbf{u}\right) = -\nabla p^* + \nabla\cdot\left[\mu(\alpha)\big(\nabla\mathbf{u} + (\nabla\mathbf{u})^T\big)\right] + \rho(\alpha)\mathbf{g} + \mathbf{f}_\sigma(\alpha,\kappa), \quad (2.1)$$

with multidimensional universal limiter with explicit solution (MULES)–compressed VOF transport and continuum surface force (CSF) surface tension (Brackbill *et al.* 1992; Scardovelli & Zaleski 1999; Rusche 2002). $\mathbf{u}$ is the mixture (volume-averaged) velocity; p^* the modified pressure; $\alpha \in [0,1]$ the water volume fraction ($\alpha = 1$ water, $\alpha = 0$ air; the interface lies near $\alpha \approx 0.5$), $\rho(\alpha) = \alpha\rho_w + (1-\alpha)\rho_a$ the phase-weighted density; $\mu(\alpha) = \alpha\mu_w + (1-\alpha)\mu_a$ the phase-weighted viscosity; $\mathbf{g}$ gravity; and $\mathbf{f}_\sigma = \sigma\,\kappa\,\nabla\alpha$ the CSF surface-tension force, with $\mathbf{n} = \nabla\alpha/|\nabla\alpha|$ and $\kappa = -\nabla\cdot\mathbf{n}$. Airside statistics are computed by masking cells with $\alpha < 0.5$.

2.2. *Signal decomposition and regression analysis*

Time series of velocity are extracted at fixed probes above the surface. To analyze turbulence and wave motion, each velocity record $u(t)$ is decomposed into high-frequency (HF) random fluctuations and a low-frequency (LF) wave coherent. We apply a fourth-order Butterworth high-pass filter (with cutoff frequency set relative to the mean wave frequency) to isolate HF fluctuations, and take the residual as LF. As an alternative, a discrete wavelet transform (DWT) decomposition is also used to remove low modes. In addition, ensemble empirical mode decomposition (EEMD) is applied to extract intrinsic mode functions (IMFs) from $u(t)$; IMFs with characteristic frequencies above the cutoff are summed as u_{HF}. Fourier transforms of $u(t)$ yield power spectra $E(f)$, averaged in time, enabling the analysis of spectral scaling. Turbulence intensities (e.g., RMS values of u') and shear velocity u_* (from log-law fits to mean profiles) are computed for each case.

To quantify statistical relationships, we perform Spearman rank correlations and regression of key metrics (e.g., RMS, integral length scales) against nondimensional parameters (e.g., wave age, fetch). Spearman coefficients identify significant monotonic trends, and a composite effects plot highlights the relative influence of wind speed and wavelength on turbulent quantities. This regression analysis is based on the processed data from the

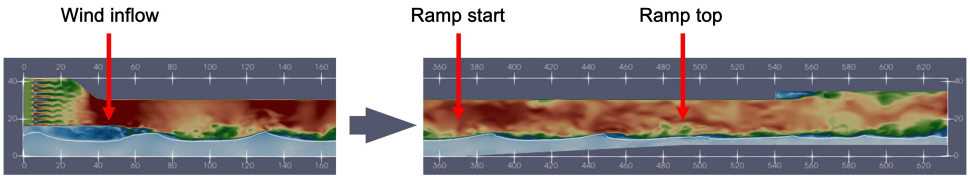

FIGURE 1. Computational domain schematic (sloping beach, flat platform) with example short wave (blue) and wind (orange arrows) for the $U = 30\,\mathrm{m/s}$ short-wave case.

Case	U_{inlet} (m/s)	Wave state	λ (m)	T (s)	Notes
u0short	0	Short	59.8212	7	Quiescent wind, short wave
u0long	0	Long	133.9051	14	Quiescent wind, long wave
u15short	15	Short	59.8212	7	Moderate wind, short wave
u15long	15	Long	133.9051	14	Moderate wind, long wave
u30short	30	Short	59.8212	7	Strong wind, short wave
u30long	30	Long	133.9051	14	Strong wind, long wave

TABLE 1. Case design (monochromatic waves; λ and T are set at the inlet).

pipeline (Butterworth/EEMD/FFT) described above Larsen *et al.* (2019); Deskos *et al.* (2021).

2.3. *Computational setup*

The computational domain consists of a flat water channel upstream followed by a linear sloped beach (slope 1:20) and a flat platform at beachcrest height. The total length is 632.84 m, with the slope extending 120 m and the platform 142.84 m (see Figure 1). The water depth on the flat is 10 m and the beachcrest is 6 m above the offshore flat bottom. The wind inflow is prescribed at the left boundary as a uniform velocity profile (either 0, 15 or 30 m/s horizontally). Surface waves are generated at the same inflow boundary using a relaxation-zone method with regular sine waves of specified amplitude and length. Six cases combine two wavelengths with three wind speeds: short (59.82 m) and long (133.91 m) wavelength waves, each with wind speed $U = 0$, 15 or 30 m/s. Figure 1 illustrates the case $U = 30\,\mathrm{m/s}$ with a short wave. Velocity probes and vertical profiles are located at several x-positions along the tank to sample wind profiles and wave heights. A no-slip condition is applied at the beach, and a stress-free top boundary. We use a moderately fine mesh ($\Delta x \approx 0.4$ m near the interface) based on prior mesh-sensitivity tests in Section 3. Further details on domain dimensions and boundary conditions are given in Table 1.

2.4. *Case design*

Six simulation cases are run, combining wind speeds $U_{inlet} = 0$, 15 and 30 m/s with two regular wave conditions (short and long wavelength). The short wave has $\lambda = 59.82$ m (period $T \approx 7$ s) and the long wave $\lambda = 133.91$ m ($T \approx 14$ s). Table 1 summarizes the cases by wind speed U_{inlet}, wavelength λ, wave period T and case label.

3. Mesh sensitivity

To ensure grid independence, we conducted mesh refinement tests. Figure 2 shows a representative flow profile (mean velocity and turbulence) for coarse ($\Delta x \approx 0.4$ m near

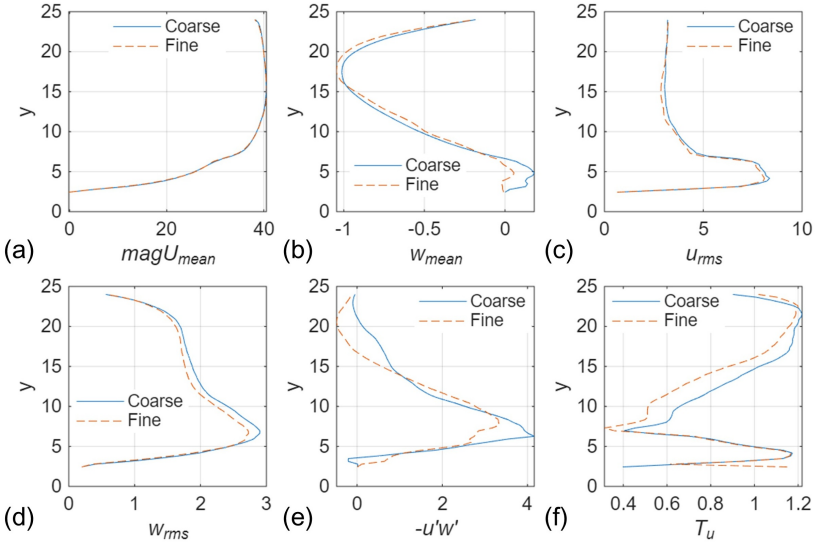

FIGURE 2. Mean velocity profile and turbulence intensity for different mesh resolutions, demonstrating negligible change in the mean flow shape.

the interface) versus fine meshes ($\Delta x \approx 0.3$ m). The merged spectra in Figure 3 compare the high-frequency energy in the flat flume, on the slope beach and on the platform across two mesh resolutions, indicating that the inertial-range scaling is consistent. Box plots in Figure 4 summarize percent changes in key metrics (mean wind, turbulent rms, shear stress $u'w'$, turbulence integral scale T_u and 90% spectral cutoff) between the baseline and finer meshes. These plots show that the mean velocity $\bar{U}$ is relatively insensitive (small relative change), while turbulent fluctuations (u_{rms}) and integral scales (T_u) exhibit larger variation. The shear stress $u'w'$ also shows some sensitivity. Based on this analysis, our chosen mesh (baseline) captures the mean flow accurately and yields acceptable convergence for turbulence statistics, with uncertainties kept within 10–20% (Figure 4). The refined mesh would increase cost significantly (increasing the number of cells from 3.7 to 8.8 million), so we adopt the baseline mesh as a compromise between accuracy and efficiency.

4. Results

4.1. *Wave height and shear velocity development*

We quantify how waves and near-surface shear evolve along the beach–platform transect by combining three diagnostics: (i) the mean wave height $h(x)$ [Figure 5(a)], (ii) the airside shear velocity $u_*(x)$ [Figure 5(b)], and (iii) a breaking score along the slope and platform [Figure 5(c)]. The along-fetch wave height $h(x)$ is obtained from the free-surface time series by pairing peaks and neighboring troughs and averaging the peak–trough distances at each probe location. As the waves shoal, $h(x)$ increases toward a local maximum near the breaker. In the no-wind cases, short waves (smaller λ) begin to break on the slope and thus peak earlier in x than long waves, whereas long waves penetrate farther shoreward before breaking. With wind forcing ($U_{inlet} = 15$ or $30\,\mathrm{m\,s^{-1}}$), peak values of h are suppressed and the post-break decay is steeper, consistent with enhanced dissipation

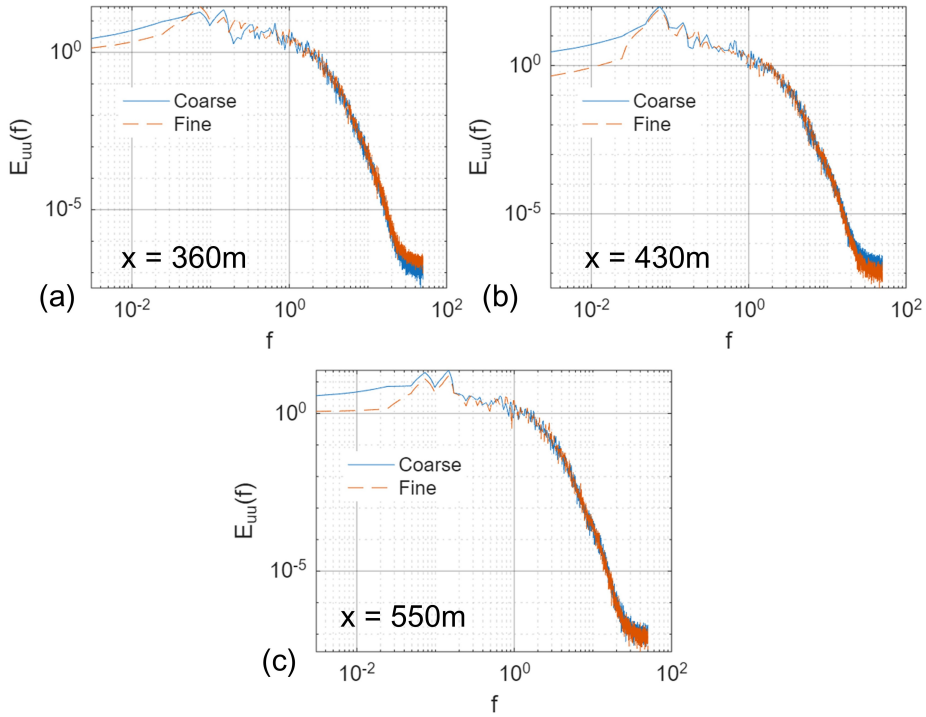

FIGURE 3. Mesh sensitivity: $E_{uu}(f)$ at three stations (baseline versus refined).

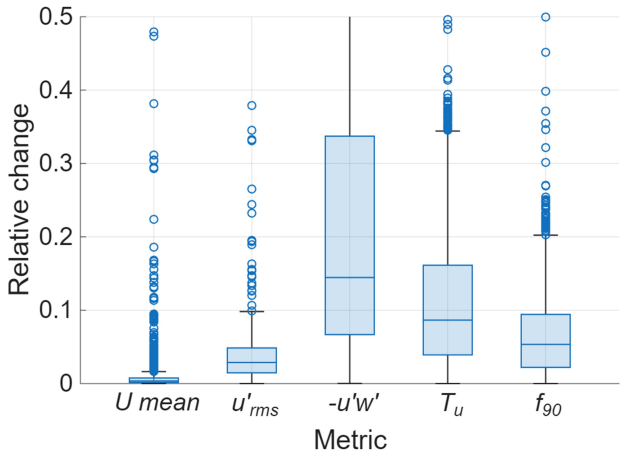

FIGURE 4. Box plots of relative changes in flow metrics when refining the mesh: U_{mean} is the mean wind velocity, u'_{rms} is velocity fluctuations, $-\overline{u'w'}$ is shear stress, T_u is an integral length scale and f_{90} is the 90% energy cutoff frequency.

by wind-augmented breaking. The airside shear velocity u_* is estimated from a log-law fit to mean wind profiles above the instantaneous surface. Specifically,

$$u_x(z) \;=\; \frac{u_*}{\kappa}\,\ln\!\left(\frac{z}{z_0}\right), \qquad u_* \;=\; \kappa\, A, \qquad z_0 \;=\; e^{-B/A}, \tag{4.1}$$

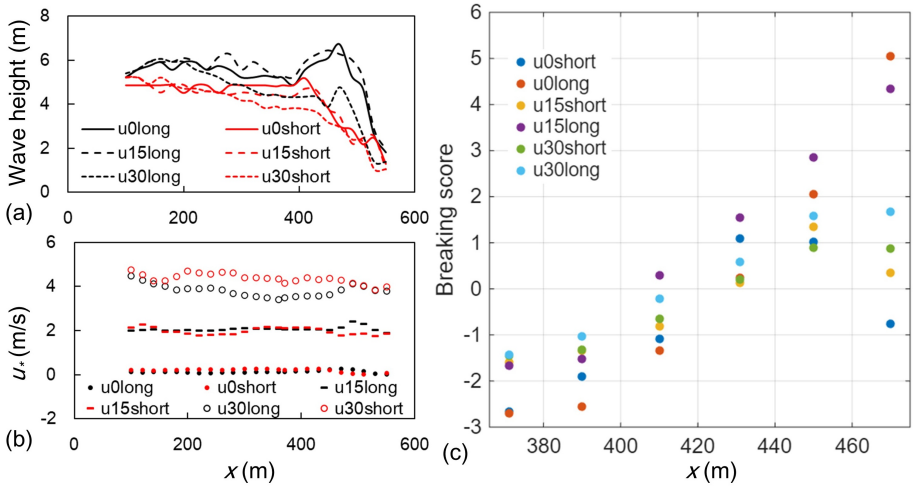

FIGURE 5. (a) Mean wave height $h(x)$; (b) shear velocity $u_*(x)$ from log-law fits; (c) standardized breaking score $S = (h/2H - \mu_{\mathcal{I}})/\sigma_{\mathcal{I}}$ along the slope and platform. The slope ends near $x \approx 370$ m. Short waves break earlier and reach peak S earlier than long waves; stronger winds suppress peak h and enhance u_*.

where $\kappa = 0.41$ is von Kármán's constant, and A, B are the slope and intercept of the least-squares fit of u_x versus $\ln z$ over a near-surface fitting layer. Across all cases, $u_*(x)$ grows toward the breaking zone—reflecting the roughening by active breakers—and is larger overall under stronger winds. Downstream of the breaker, u_* gradually relaxes as wave height diminishes. To localize breaking on the slope, we first form a raw crest–depth ratio,

$$S_{\mathrm{raw}}(x) \;=\; \frac{a(x)}{H(x)} \;=\; \frac{h(x)}{2H(x)}, \tag{4.2}$$

where $a = h/2$ is the crest amplitude and $H(x)$ is the local water depth. Values of S_{raw} peak near the breaker, typically approaching 0.8–0.9 at onset. For cross-case comparison in the right panel, we plot a standardized score

$$S(x) \;=\; \frac{S_{\mathrm{raw}}(x) - \mu_{\mathcal{I}}}{\sigma_{\mathcal{I}}}, \tag{4.3}$$

where $\mu_{\mathcal{I}}$ and $\sigma_{\mathcal{I}}$ are, respectively, the mean and standard deviation of S_{raw} computed over the slope–platform interval $\mathcal{I}$. This normalization collapses case-to-case offsets and yields the range seen in Figure 5 (c). Short-wave cases attain larger positive S earlier in x, indicating earlier and stronger breaking; stronger winds modestly shift the maxima upslope and reduce the post-break $h(x)$. Together, the panels show that wavelength primarily sets the breaking location and decay of $h(x)$, while wind strength governs the magnitude of $u_*(x)$ and the severity of post-break attenuation. High $S(x)$ coincides with elevated $u_*(x)$, consistent with enhanced air–sea momentum exchange over breaking waves.

4.2. *Mean velocity and turbulence profiles*

Figures 6 and 7 compare mean wind speed magnitude $|\mathbf{U}|$ and RMS velocity fluctuations above the surface in two regions: upstream of the slope (flat zone) and on the slope plateau. The pre-slope shows a near-neutral boundary layer over the flat: The mean pro-

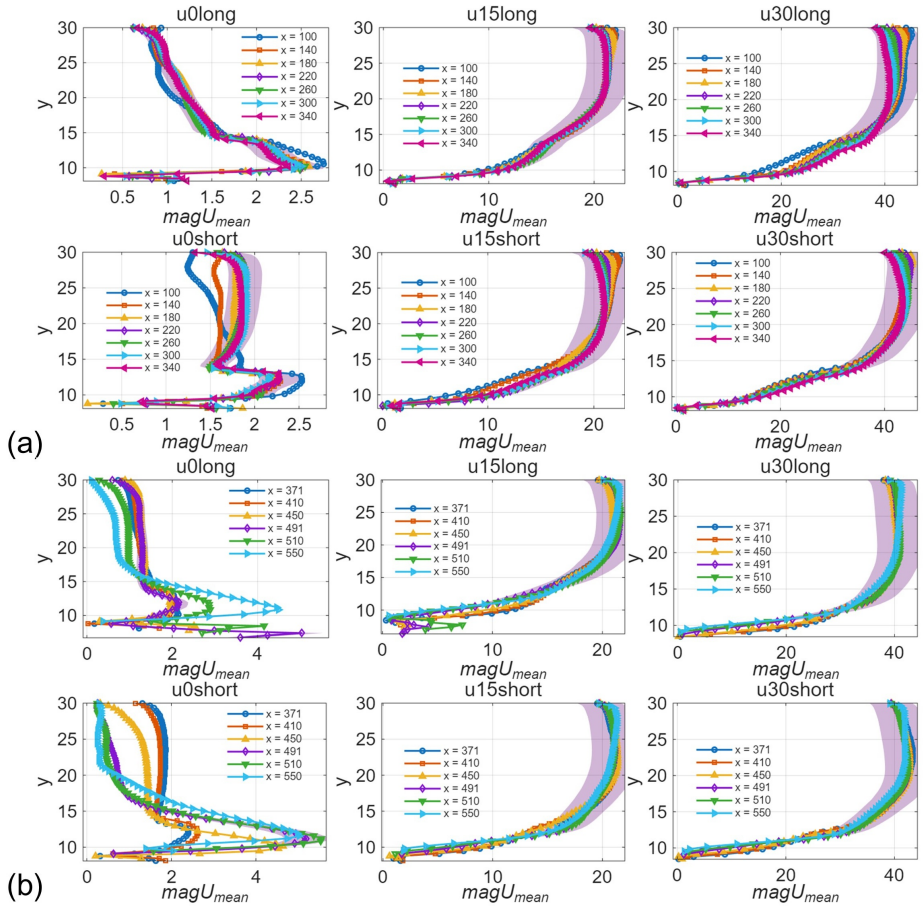

FIGURE 6. Mean velocity magnitude profiles (a) upstream of the slope and (b) on slope and platform.

file roughly follows a logarithmic shape, with lower turbulence (u'_{rms}) near the surface. On the sloped section, the wind slows near the crest and flow decelerates upslope, so the velocity profile is bent downward (smaller near-surface $|\mathbf{U}|$). Turbulent intensity is higher on the slope due to wave forcing: u'_{rms} is elevated throughout the depth and peaks near the crest. For example, in the $U = 30$ m/s cases, the ramp profiles show a thicker turbulent layer and higher u'_{rms} compared to the flat. Comparing short versus long waves, the short-wave cases exhibit a more pronounced turbulence peak on the slope, reflecting stronger breaking. Overall, the wind profile upstream is relatively undisturbed, but after encountering the breaking waves, the flow becomes more turbulent and decelerated, especially in the crest region.

4.3. *Spectra and integral length scales*

Figure 8 shows power spectra of the velocity at a representative height. The spectra follow an approximate $-5/3$ slope in the inertial subrange and display a peak at the wave-forcing frequency. Under breaking, the high-frequency tail is amplified, indicating the generation of small scales. Both wind and waves shape the spectrum: Cases with stronger wind have slightly more energy at all scales.

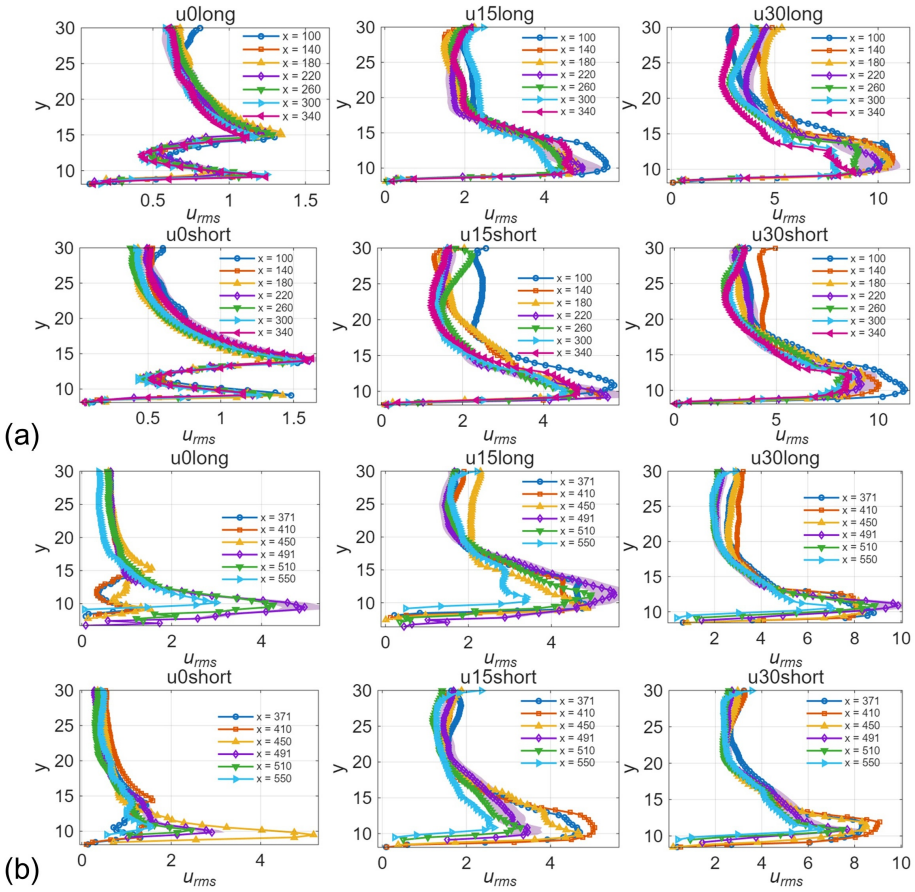

FIGURE 7. RMS profiles of streamwise fluctuations (a) upstream of the slope and (b) on slope and platform.

Figures 9 and 10 plot the integral length scale (ILS) at two heights (5 m and 13 m above the mean surface) for each case. The ILS is computed from the autocorrelation function of u' and represents the size of the largest eddies. We find that near the surface (5 m), the ILS is generally smaller than aloft, reflecting smaller turbulent eddies from wave breaking. On the slope (higher x), the ILS increases with height and with longer waves, as longer waves produce larger-scale motions. On the flat platform, ILS tends to decrease downwind for all cases. In summary, shorter waves produce smaller length scales, and higher wind tends to slightly increase the ILS due to stronger shear-driven eddies. These variations indicate that wave breaking generates turbulence of a scale comparable to the local water depth [consistent with Thomson *et al.* (2016)], while farther above the surface the eddies grow larger.

4.4. *Regression analysis*

Figure 11 presents a Spearman rank-correlation matrix between key parameters (wind speed U_{inlet}, wave age u_*/c, fetch x/λ etc.) and response metrics (shear stress $-u'w'$, RMS and ILS). Strong correlations (yellow or orange) indicate that U_{inlet} and wave age have the greatest influence on near-surface turbulence and u_*. For example, $-u'w'$ and

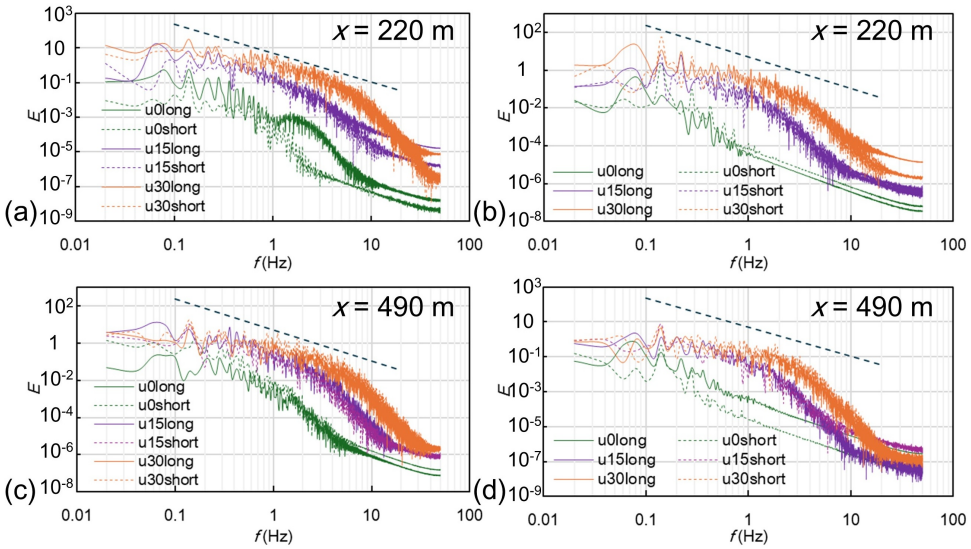

FIGURE 8. Energy spectra of the high-frequency velocity component (log–log) for all cases at (a,c) 5m above the mean water surface and (b,d) 13m above the mean water surface. Breaking introduces extra energy at high wave numbers (right tail).

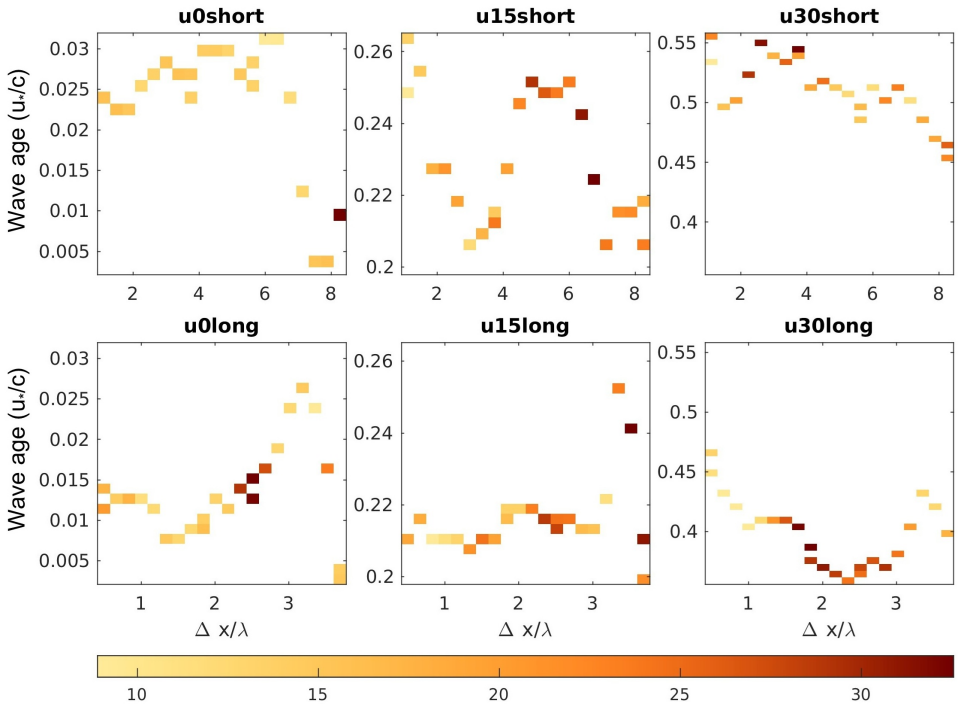

FIGURE 9. Integral length scale (ILS) of turbulence at 5 m above surface versus streamwise position for each case. Values are smaller near the surface and increase over the slope before decreasing on the flat. Long-wave cases have larger ILS than short-wave cases.

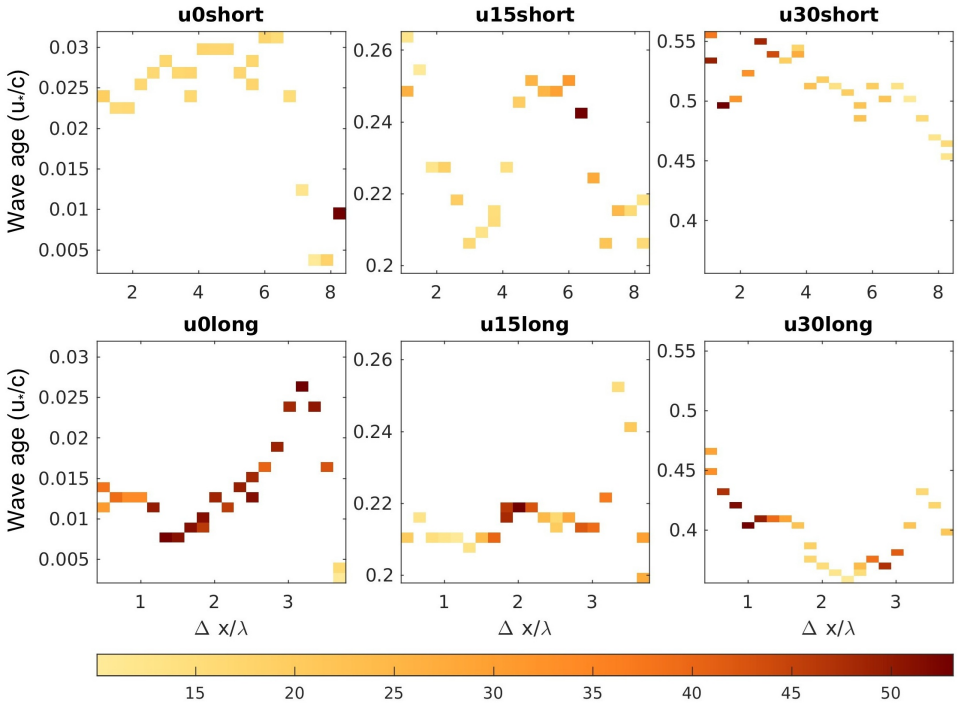

FIGURE 10. Integral length scale at 13 m height. All cases have larger ILS aloft compared to near-surface values (Figure 9). The trends are similar: Eddies grow over the slope and shrink on the platform.

u'_{rms} correlate positively with U_{inlet} ($r \approx 0.8$). The composite effects figure (Figure 12) quantifies these trends: Increasing wind speed raises turbulence intensity, while longer waves (higher wave age) tend to increase wave breaking depth and mixing. In contrast, increasing normalized fetch x/λ (farther downwind) generally reduces turbulence, as waves have already broken. Overall, the regression confirms that wind speed and wave age are the dominant factors controlling shear-driven turbulence in this slope–platform setup.

5. Conclusions

Simulations of wind-driven waves on a sloping beach show that wave breaking and airflow turbulence are closely coupled. Waves shoal and break on the slope, with short waves breaking earlier and dissipating more energy. Breaking significantly enhances near-surface turbulence, confined to a shallow layer [consistent with observations Thomson *et al.* (2016)]. Stronger winds increase shear and turbulence, generally reducing wave height due to more vigorous breaking. The mean wind profile adjusts after the breaker zone, slowing near the surface and thickening the boundary layer. Spectral and length-scale analysis indicate that breaking injects energy into smaller scales and that the largest eddies grow aloft. Regression analysis confirms that wind speed and wave age are the main drivers of the observed turbulence levels. These results provide insight into the detailed flow structure in a coastal wind–wave environment, relevant for coastal engineering and air–sea coupling models.

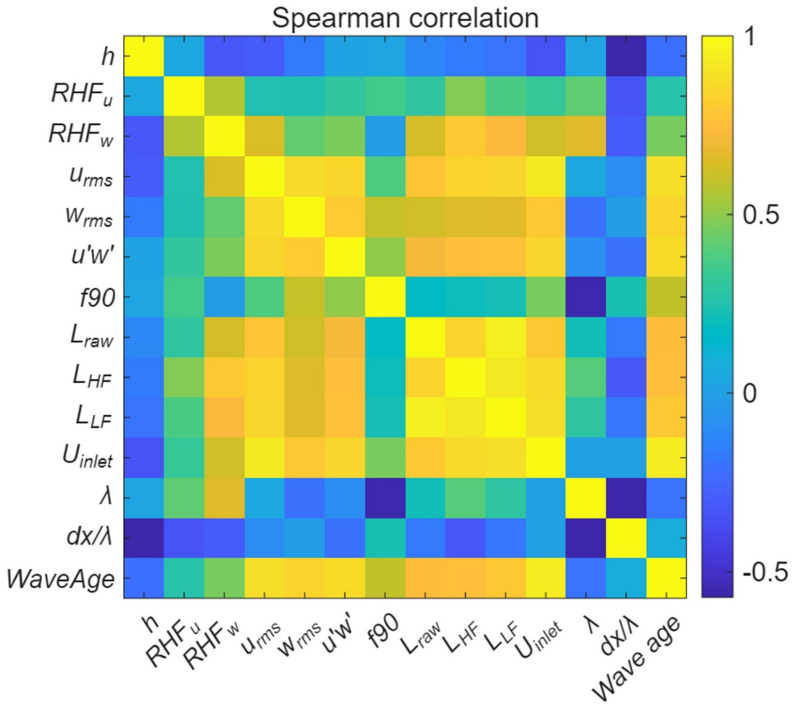

FIGURE 11. Spearman correlation coefficients between inputs and output metrics. Significant correlations occur between wind speed/wave age and turbulence quantities.

Acknowledgments

This report is based upon work supported by NSF Award CMMI- 2131961. Some of the computing for this project was performed on the Sherlock cluster.

REFERENCES

BANNER, M. L. & PEIRSON, W. L. 2007 Wave breaking onset and strength for two-dimensional deep-water waves. *J. Fluid Mech.* **585**, 93–115.

BELCHER, S. E. & HUNT, J. C. R. 1993 Turbulent flow over hills and waves. *Annu. Rev. Fluid Mech.* **25**, 507–538.

BRACKBILL, J. U., KOTHE, D. B. & ZEMACH, C. 1992 A continuum method for modeling surface tension. *J. Comput. Phys.* **100**, 335–354.

BUCKLEY, M. P. & VERON, F. 2016 Structure of the airflow above surface waves. *J. Phys. Oceanogr.* **46**, 1377–1397.

CHARNOCK, H. 1955 Wind stress on a water surface. *Q. J. R. Meteorol. Soc.* **81**, 639–640.

DESKOS, G., LEE, J. C. Y., DRAXL, C. & SPRAGUE, M. A. 2021 Review of wind–wave coupling models for large-eddy simulation of the marine atmospheric boundary layer. *J. Atmos. Sci.* **78**, 3025–3037.

HAO, X. & SHEN, L. 2019 Wind–wave coupling study using les of wind and phase-resolved simulation of nonlinear waves. *J. Fluid Mech.* **874**, 391–425.

HARA, T. & BELCHER, S. E. 2004 Wind profile and drag coefficient over mature ocean surface wave spectra. *J. Phys. Oceanogr.* **34**, 234–248.

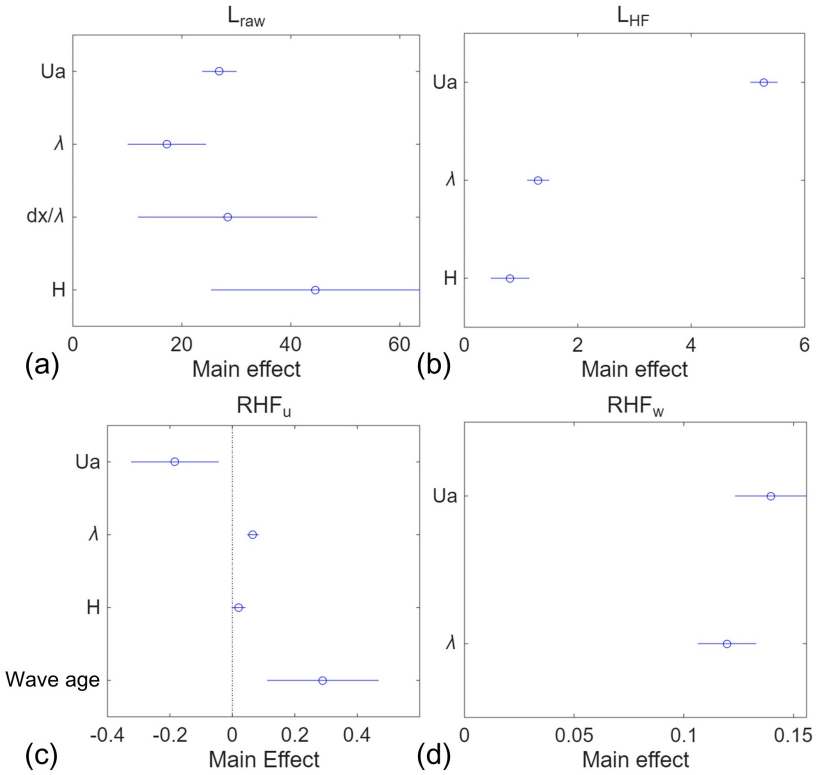

FIGURE 12. Partial effects from stepwise linear models with interactions.

HIRT, C. W. & NICHOLS, B. D. 1981 Volume of fluid (vof) method for the dynamics of free boundaries. *J. Comput. Phys.* **39**, 201–225.

LARSEN, B. E., FUHRMAN, D. R. & ROENBY, J. 2019 Performance of `interFoam` on the simulation of progressive waves. *Coast. Eng. J.* **61**, 380–400.

MELVILLE, W. K. 1996 The role of surface-wave breaking in air–sea interaction. *Annu. Rev. Fluid Mech.* **28**, 279–321.

MILES, J. W. 1957 On the generation of surface waves by shear flows. *J. Fluid Mech.* **3**, 185–204.

PHILLIPS, O. M. 1957 On the generation of waves by turbulent wind. *J. Fluid Mech.* **2**, 417–445.

PHILLIPS, O. M. 1985 Spectral and statistical properties of the equilibrium range in wind-generated gravity-waves. *J. Fluid Mech.* **156**, 505–531.

POPINET, S. 2009 An accurate adaptive solver for surface-tension-driven interfacial flows. *J. Comput. Phys.* **228**, 5838–5866.

ROMERO, L., MELVILLE, W. K. & KLEISS, J. M. 2012 Spectral energy dissipation due to surface wave breaking. *J. Phys. Oceanogr.* **42**, 1421–1444.

RUSCHE, H. 2002 Computational fluid dynamics of dispersed two-phase flows at high phase fractions. PhD thesis, Imperial College London, London, United Kingdom.

SCARDOVELLI, R. & ZALESKI, S. 1999 Direct numerical simulation of free-surface and interfacial flow. *Annu. Rev. Fluid Mech.* **31**, 567–603.

SULLIVAN, P. P., EDSON, J. B., HRISTOV, T. & MCWILLIAMS, J. C. 2000 Large-

eddy simulations and observations of atmospheric marine boundary layers above nonequilibrium surface waves. *J. Atmos. Sci.* **65**, 1225–1245.

Sullivan, P. P. & McWilliams, J. C. 2010 Dynamics of winds and currents coupled to surface waves. *Annu. Rev. Fluid Mech.* **42**, 19–42.

Thomson, J., Schwendeman, M. S., Zippel, S. F., Moghimi, S., Gemmrich, J. & Rogers, E. W. 2016 Wave-breaking turbulence in the ocean surface layer. *J. Phys. Oceanogr.* **46**, 1857–1870.

Veron, F. 2015 Ocean spray. *Annu. Rev. Fluid Mech.* **47**, 507–538.

Weller, H. G., Tabor, G., Jasak, H. & Fureby, C. 1998 A tensorial approach to computational continuum mechanics using object-oriented techniques. *Comput. Phys.* **12**, 620–631.